Lu *et al. Journal of Nanobiotechnology* (2022) 20:350
https://doi.org/10.1186/s12951-022-01562-y

Journal of Nanobiotechnology

RESEARCH

Open Access

Biodegradable and biocompatible exceedingly small magnetic iron oxide nanoparticles for T_1-weighted magnetic resonance imaging of tumors

Xuanyi Lu[1†], Huimin Zhou[2†], Zhiyu Liang[3], Jie Feng[3], Yudie Lu[1], Lin Huang[1], Xiaozhong Qiu[2*], Yikai Xu[3*] and Zheyu Shen[1,2,3*]

Abstract

Magnetic resonance imaging (MRI) has been widely using in clinical diagnosis, and contrast agents (CAs) can improve the sensitivity MRI. To overcome the problems of commercial Gd chelates-based T_1 CAs, commercial magnetic iron oxide nanoparticles (MIONs)-based T_2 CAs, and reported exceedingly small MIONs (ES-MIONs)-based T_1 CAs, in this study, a facile co-precipitation method was developed to synthesize biodegradable and biocompatible ES-MIONs with excellent water-dispersibility using poly (aspartic acid) (PASP) as a stabilizer for T_1-weighted MRI of tumors. After optimization of the synthesis conditions, the final obtained ES-MION9 with 3.7 nm of diameter has a high r_1 value (7.0 ± 0.4 mM^{-1} s^{-1}) and a low r_2/r_1 ratio (4.9 ± 0.6) at 3.0 T. The ES-MION9 has excellent water dispersibility because of the excessive –COOH from the stabilizer PASP. The pharmacokinetics and biodistribution of ES-MION9 in vivo demonstrate the better tumor targetability and MRI time window of ES-MION9 than commercial Gd chelates. T_1-weighted MR images of aqueous solutions, cells and tumor-bearing mice at 3.0 T or 7.0 T demonstrate that our ES-MION9 has a stronger capability of enhancing the MRI contrast comparing with the commercial Gd chelates. The MTT assay, live/dead staining of cells, and H&E-staining indicate the non-toxicity and biosafety of our ES-MION9. Consequently, the biodegradable and biocompatible ES-MION9 with excellent water-dispersibility is an ideal T_1-weighted CAs with promising translational possibility to compete with the commercial Gd chelates.

Keywords: Magnetic resonance imaging (MRI), Contrast agents (CAs), Exceedingly small magnetic iron oxide nanoparticles (ES-MIONs), Poly (aspartic acid) (PASP), Biodegradable

Introduction

Magnetic resonance imaging (MRI) has been widely using in clinical diagnosis and prognosis observation to distinguish lesions from normal tissues, especially for the diagnosis of tumors, because of its obvious superiorities, including high soft tissue contrast, high spatial resolution, non-invasion and non-radiation [1–4]. Contrast agents (CAs) play an indispensable role to enhance the sensitivity of MRI. T_1-weighted CAs (i.e., positive CAs) can shorten the proton's longitudinal relaxation time (T_1) to produce brighter images, while T_2-weighted CAs (i.e.,

---

†Xuanyi Lu and Huimin Zhou contributed equally to this work

*Correspondence: qqiuxzh@163.com; yikaivip@163.com; sz@smu.edu.cn

[1] Biomaterials Research Center, School of Biomedical Engineering, Southern Medical University, 1023 Shatai South Road, Guangzhou 510515, Guangdong, China
[2] Guangdong Provincial Key Laboratory of Construction and Detection in Tissue Engineering, School of Basic Medical Sciences, Southern Medical University, 1023 Shatai South Road, Guangzhou 510515, Guangdong, China
[3] Medical Imaging Center, Nanfang Hospital, School of Biomedical Engineering, Southern Medical University, 1023 Shatai South Road, Guangzhou 510515, Guangdong, China

© The Author(s) 2022. **Open Access** This article is licensed under a Creative Commons Attribution 4.0 International License, which permits use, sharing, adaptation, distribution and reproduction in any medium or format, as long as you give appropriate credit to the original author(s) and the source, provide a link to the Creative Commons licence, and indicate if changes were made. The images or other third party material in this article are included in the article's Creative Commons licence, unless indicated otherwise in a credit line to the material. If material is not included in the article's Creative Commons licence and your intended use is not permitted by statutory regulation or exceeds the permitted use, you will need to obtain permission directly from the copyright holder. To view a copy of this licence, visit http://creativecommons.org/licenses/by/4.0/. The Creative Commons Public Domain Dedication waiver (http://creativecommons.org/publicdomain/zero/1.0/) applies to the data made available in this article, unless otherwise stated in a credit line to the data.

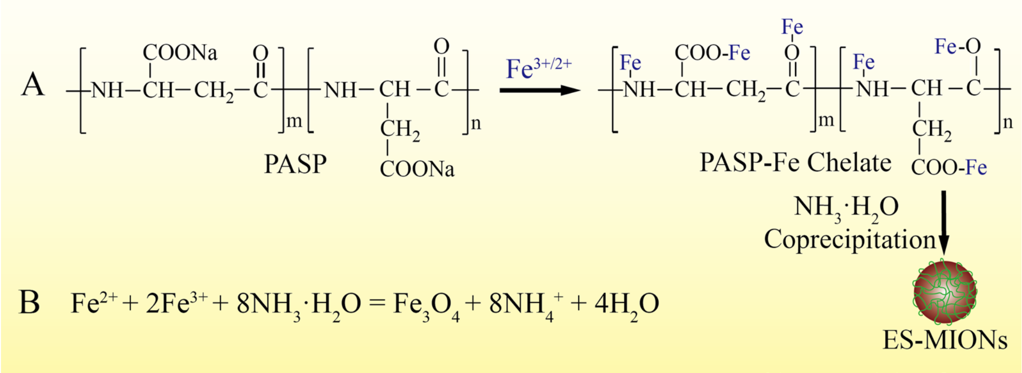

$$Fe^{2+} + 2Fe^{3+} + 8NH_3 \cdot H_2O = Fe_3O_4 + 8NH_4^+ + 4H_2O$$

Scheme 1 Schematic illustration of synthesis process (**A**) and reaction equation (**B**) for the ES-MIONs

negative CAs) can shorten proton's transverse relaxation time (T_2) to generate darker images [5–8]. Currently, most clinical T_1 CAs are gadolinium (Gd) chelates, including Magnevist (Gd-DTPA), Gadavist (Gd-DO3A-Butriol), Dotarem (Gd-DOTA), Eovist (Gd-EOB-DTPA), Omniscan (Gd-DTPA-BMA), and so on [9–12]. However, the U.S. food and drug administration (FDA) has warned that the Gd chelates tend to cause nephrogenic system fibrosis and cerebral deposition [13–15]. In addition, the T_1 imaging capability of the commercial Gd chelates is not strong due to their small longitudinal relaxivity (r_1, ~ 4 mM^{-1} s^{-1}) [16].

In order to overcome the problems of Gd chelates, increasing studies have been focusing on magnetic iron oxide nanoparticles (MIONs) due to their excellent biocompatibility [17–20]. Actually, MIONs were first used as T_2-weighted CAs for examination of human liver in 1994 [21]. Several types of MIONs, such as Supravist, Feridex, and Rsovist, were developed and used as T_2 CAs for MRI of human diseases in the 2000s [22]. However, these MION agents are not used in clinic anymore due to the following problems. (1) The MION agents produce darker MR images that are not conducive to the clinician's diagnosis for diseases [23]. (2) Slow body clearance and long blood circulation lead to long waiting time for patients. (3) The high magnetic moment of MIONs can result in susceptibility artifacts. (4) The long echo time (TE) and repetition time (TR) result in long processing time of clinical MRI examinations. (5) Eovist, a liver-specific T_1 contrast agent, was approved in 2008, and used to replace the MIONs-based T_2 CAs.

Because there are no ideal products in clinic, MRI CAs have been one of the research hotspots for a long time. The recently emerging ES-MIONs (< 5.0 nm) with high r_1 and low transversal relaxivity (r_2) can be used as T_1 CAs without concerns of nephrotoxicity and cerebral deposition [24–26]. Therefore, ES-MIONs can surmount drawbacks of the above-mentioned Gd chelates and MIONs. Kim et al. reported uniform ES-MIONs prepared by a method of thermal decomposition in 2011, which has low r_2 value [27]. However, the ES-MIONs synthesized in oil phase are not soluble in water and need further hydrophilic functionalization on their surfaces, which severely limits their clinical applications. To solve this problem, we previously synthesized ES-MIONs with stabilization of poly (acrylic aid) (PAA) in aqueous phase by co-precipitation method [23]. The synthesized ES-MIONs can be easily dispersed in water, and the dispersion can be kept at room temperature for several months without any precipitation. However, the used stabilizer PAA is not biodegradable in human physiological environment.

In this study, a facile co-precipitation method was developed to synthesize biodegradable and biocompatible ES-MIONs (< 5.0 nm) with excellent water-dispersibility for T_1-weighted MRI of tumors. As shown in Scheme 1A, biodegradable poly (aspartic acid) (sodium salt, PASP) first react with Fe^{3+} and Fe^{2+} to form PASP-Fe chelate, which can further react with ammonia solution producing biodegradable and biocompatible ES-MIONs via co-precipitation. The reaction equation generating Fe_3O_4 is shown in Scheme 1B. Due to the enrichment of carboxyl groups in the surface, the negatively charged ES-MIONs have excellent water-dispersibility. Because the amide bonds of PASP are biodegradable in human physiological environment, PASP can be used as an excellent candidate as the stabilizer for the synthesis of ES-MIONs. The PASP cannot be replaced with other poly(amino acids) because they are either less water-soluble than PASP, or positively charged. Because the r_1 value (7.0 mM^{-1} s^{-1}) is much higher than that of commercial Gd chelates (~ 4 mM^{-1} s^{-1}) and the iron is one of the essential elements in the human body, the obtained ES-MIONs are biocompatible and have huge potential to be used as T_1 MRI CAs, surpassing the commercial Gd chelates.

Results and discussion

Synthesis and characterization of ES-MIONs

The ES-MIONs were synthesized by a method of co-precipitation, and reaction conditions were optimized to obtain high quality ES-MIONs with high r_1 and r_2/r_1 (Additional file 1: Table S1). PASP was used as a stabilizer for the ES-MIONs preparation, which gives the obtained ES-MIONs excellent water dispersibility. Four concentrations of PASP solutions were used for synthesis of ES-MION1-4. The Fe concentration of ES-MIONs was determined by inductively coupled plasma-optical emission spectrometry (ICP-OES), and the ES-MION2 has the largest Fe recovery of 96.6% (Additional file 1: Table S1). T_1 and T_2 relaxation rates (3.0 T) versus Fe concentration of ES-MION1-4 are shown in Fig. 1A, B. The r_1 and r_2 values are obtained from the linear line slopes, which are summarized in Fig. 1E and Additional file 1: Table S1. The ES-MION2 has a r_1 value of 1.6 $\mathrm{mM}^{-1}\ \mathrm{s}^{-1}$ and r_2/r_1 ratio of 8.8. Though the r_1 of ES-MION3, 4 is larger than ES-MION2, the r_2/r_1 values of ES-MION3, 4 are also much higher than that of ES-MION2, which are not good for T_1 imaging. The r_2/r_1 value of ES-MION1 is lower than that of ES-MION2, but the r_1 value is also lower than that of ES-MION2. Therefore, 2.0 mg/mL of PASP solution was considered as the optimal concentration for the synthesis of ES-MIONs.

Furthermore, 0.5–8.0% of ammonia solutions were used to synthesize ES-MION5-8, whose T_1 and T_2 relaxation rates (3.0 T) as a function of Fe concentration are shown in Fig. 1C, D. As shown in Fig. 1F and Additional file 1: Table S1, the r_1 and r_2/r_1 of ES-MION6 are comparable to those of ES-MION5, but much better than ES-MION 7, 8. Therefore, 4.0% of ammonia solution was chosen as the optimal condition.

In addition, based on the optimized conditions for ES-MION6 synthesis, the concentration of PASP and iron precursors ($\mathrm{FeCl_3}$ plus $\mathrm{FeSO_4}$) were all decreased to synthesize ES-MION9-11. From Fig. 1C, D, F and Additional file 1: Table S1, it can be found that ES-MION9 has a highest r_1 value of 7.0 ± 0.4 $\mathrm{mM}^{-1}\ \mathrm{s}^{-1}$ (3.0 T) and a lowest r_2/r_1 value of 4.9 ± 0.6 (3.0 T) compared with ES-MION6, 10, 11. According to Eq. (1) [28], the signal intensity of MRI is depended on gradient intensity ($\mathrm{M_0}$), echo time (TE), repetition time (TR), flip Angle (α), $\mathrm{R_2}^*$ and $\mathrm{R_1}$. The factors of $\mathrm{M_0}$, TE, TR, and α could be regulated by MRI scanners, while $\mathrm{R_2}^*$ and $\mathrm{R_1}$ depend on contrast agents. The $\mathrm{R_2}^*$ can be considered a valid $\mathrm{R_2}$ and is always greater than or equal to $\mathrm{R_2}$. It can be concluded that the $\mathrm{T_1}$ MRI signal intensity is proportional to r_1 value, but inversely proportional to r_2/r_1 ratio. Thus, the synthesis conditions of ES-MION9 should be optimal to obtain a high $\mathrm{T_1}$ MRI capability with a high r_1 and low r_2/r_1.

$$\text{Signal intensity} = \mathrm{M_0}\sin(\alpha)\frac{1-\mathrm{e}^{-\mathrm{R_1}\cdot\mathrm{TR}}}{1-\cos(\alpha)\cdot\mathrm{e}^{-\mathrm{R_1}\cdot\mathrm{TR}}}\mathrm{e}^{-\mathrm{R_2^*}\cdot\mathrm{TE}} \tag{1}$$

Besides, Fe recoveries of ES-MION1-11 tested by ICP-OES are all above 85%, indicating high utilization rates of raw materials and low cost for ES-MIONs synthesis, which are beneficial for clinical transformation.

According to previous reports, $\mathrm{Fe_3O_4}$ nanoparticles with size below 5.0 nm can be used as T_1 CAs [24]. Furthermore, $\mathrm{Fe_3O_4}$ nanoparticles with large particle size are easily taken up by the spleen and liver, which seriously affects tumor images. The images of transmission electron microscopy (TEM, Fig. 2A–K) indicate our ES-MION1-11 have excellent water dispersibility. It is found from the TEM images (Fig. 2A–D) and size distributions (Additional file 1: Fig. S1A–D) measured from TEM images that the concentration of PASP has a large influence on the sizes of ES-MIONs. The sizes of ES-MION1-4 are respectively 2.7, 2.5, 6.0 and 8.0 nm, whose r_1 is 1.0, 2.0, 4.7, and 5.4 $\mathrm{mM}^{-1}\ \mathrm{s}^{-1}$, and the r_2/r_1 is 1.9, 7.0, 19.0, and 28.3. These results demonstrate that $\mathrm{Fe_3O_4}$ nanoparticles with size below 5.0 nm have potential as T_1 CAs, while those with size larger than 5.0 nm can be only utilized as T_2 CAs due to the high r_2/r_1 ratios. Figure 2E–K and Additional file 1: Fig. S1E–K show that both the concentration of ammonia solution and the whole concentrations of feeding materials have a slight influence on the size of ES-MIONs. The relationships between the particle size and r_1 value (or r_2/r_1 ratio) (Fig. 2L) show that the best particle size is 3.7 nm (ES-MION9).

Three batches of ES-MION9 were synthesized and the T_1/T_2 relaxation rates were determined by a 3.0 T (Additional file 1: Fig. S2) and 7.0 T MRI scanner (Additional file 1: Fig. S3), whose similar r_1 and r_2 data for different batches demonstrate the good repeatability for ES-MION9 synthesis. At 3.0 T, the ES-MION9 has a larger r_1 (7.0 ± 0.4 $\mathrm{mM}^{-1}\ \mathrm{s}^{-1}$) than Gadavist ($4.9 \pm 0.1$ $\mathrm{mM}^{-1}\ \mathrm{s}^{-1}$), indicating a stronger $\mathrm{T_1}$ MRI capability of our ES-MION9.

The related T_1-weighted MR images (3.0 T) of ES-MION1-11 are shown in Additional file 1: Figs. S4A, S5A, and S6A. The corresponding SNR and ΔSNR values were calculated according to Eqs. (2) and (3) [29, 30], and shown in Additional file 1: Figs. S4B, S5B, and S6B, which reinforce that the signal intensities of MR images increase with the increase of Fe concentration with a strong concentration gradient dependence, showing good T_1-weighted MR capabilities of ES-MION1-11.

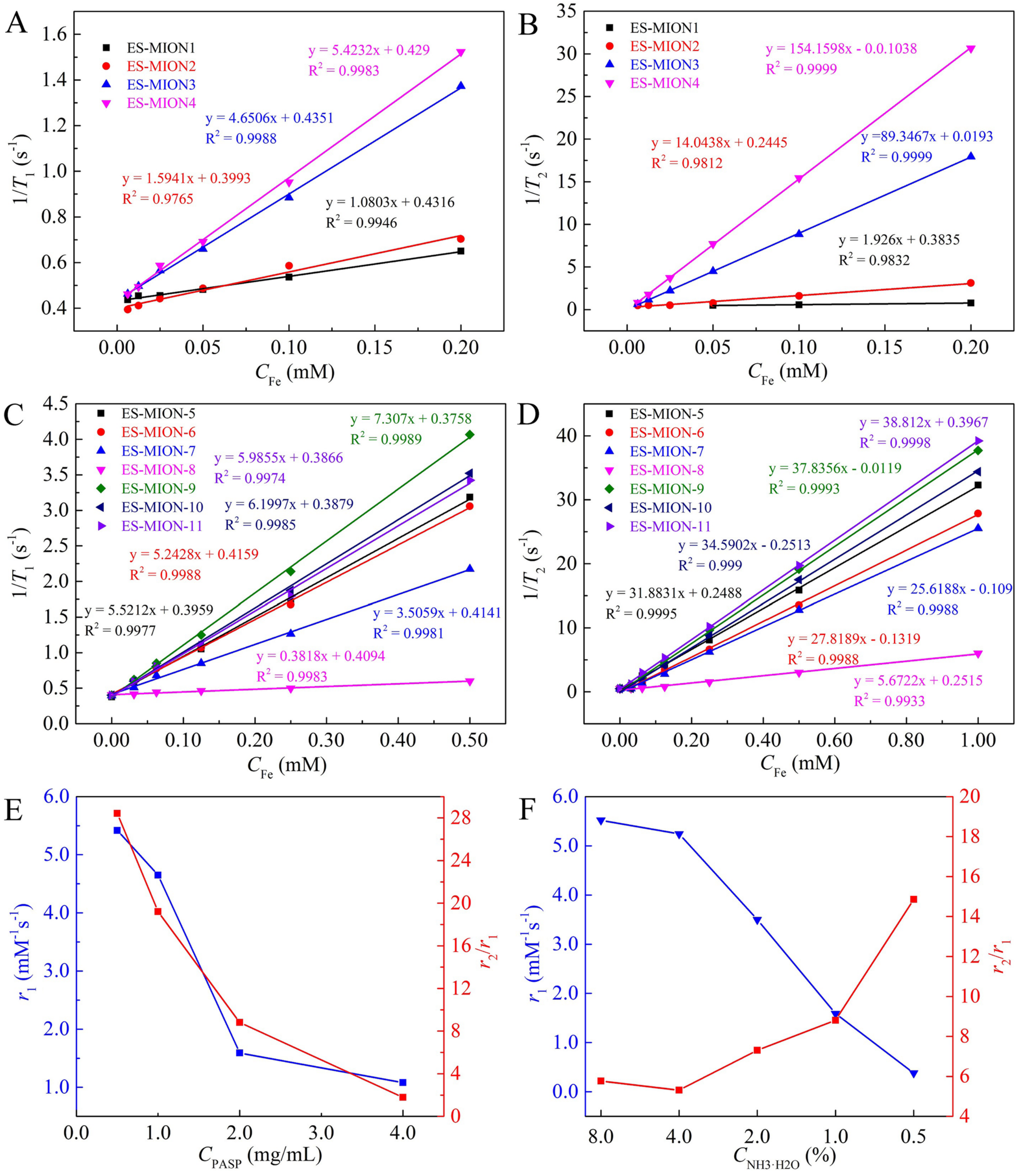

Fig. 1 **A**–**D** T_1 relaxation rate ($1/T_1$) (**A**, **C**) or T_2 relaxation rate ($1/T_2$) (**B**, **D**) plotted versus C_{Fe} for ES-MION1-11. **E**, **F** The r_1 or r_2/r_1 of the ES-MION1-4 (**E**) or ES-MION5-8 (**F**) as a function of C_{PASP} or $C_{NH3\cdot H2O}$. The magnetic field is 3.0 T

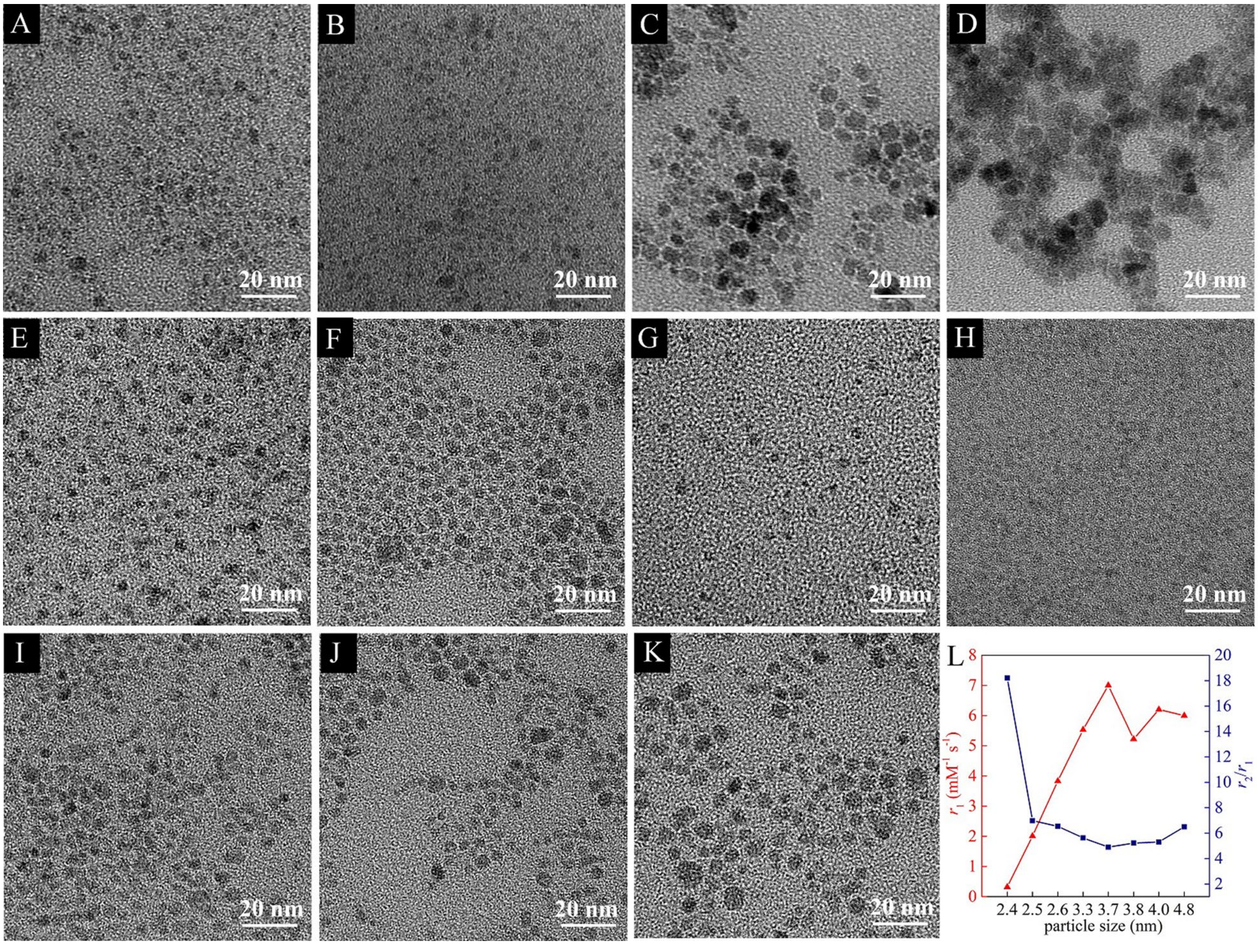

Fig. 2 **A**–**K** TEM images of ES-MION1-11. **L** The r_1 and r_2/r_1 of ES-MIONs plotted versus its diameter

$$\mathrm{SNR} = \frac{\mathrm{SI}_{\mathrm{mean}}}{\mathrm{SD}_{\mathrm{noise}}} \tag{2}$$

$$\Delta\mathrm{SNR} = \frac{(\mathrm{SNR}_{\mathrm{sample}} - \mathrm{SNR}_{\mathrm{control}})}{\mathrm{SNR}_{\mathrm{control}}} \times 100\% \tag{3}$$

It is obvious that the ΔSNR value of ES-MION9 is the maximum up to 5500% when the Fe concentration of is 1.0 mM (Additional file 1: Fig. S6B), which further demonstrate 3.7 nm is the best diameter of ES-MIONs for T_1 MRI.

The T_1 images (3.0 T) of ES-MION9 solution at 1.0 mM were further compared with the commercial Gadavist at 1.0 mM of Gd concentration (Fig. 3A). It can be seen from Fig. 3B that the ΔSNR (5400%) of ES-MION9 is higher than that (4600%) of Gadavist (***P < 0.001), which demonstrates the better MR imaging capability of our ES-MION9 (r_1 is 7.0 mM^{-1} s^{-1}, r_2/r_1 is 4.9, 3.0 T) compared with the Gadavist.

A 7.0 T of MRI scanner was also used to double confirm the T_1-weighted MRI contrast of ES-MION9 solutions at various concentrations compared with pure water (Additional file 1: Fig. S7A). The corresponding ΔSNR values (Additional file 1: Fig. S7B) also show a strong concentration gradient dependence, indicating a strong MRI capability at 7.0 T.

The ES-MION9 HR-TEM image is presented in Additional file 1: Fig. S8A. The lattice planes of 311 and 220 can be confirmed by the 0.51 and 0.301 nm of interplanar distances [31], indicating a crystalline structure of ES-MION9. The characteristic peaks of O and Fe can be found in the EDS (Additional file 1: Fig. S8B), demonstrating the component of iron oxide for ES-MION9 [32]. To further demonstrate the successful synthesis of Fe_3O_4 nanoparticles, the X-ray photoelectron spectroscopy (XPS) of ES-MION9 is performed in Additional file 1: Fig. S8C. The primary peaks at 723.8 and 710.3 eV correspond to the energy of Fe 2p3/2 and Fe 2p1/2 [33, 34], indicating the Fe_3O_4 component of our ES-MION9

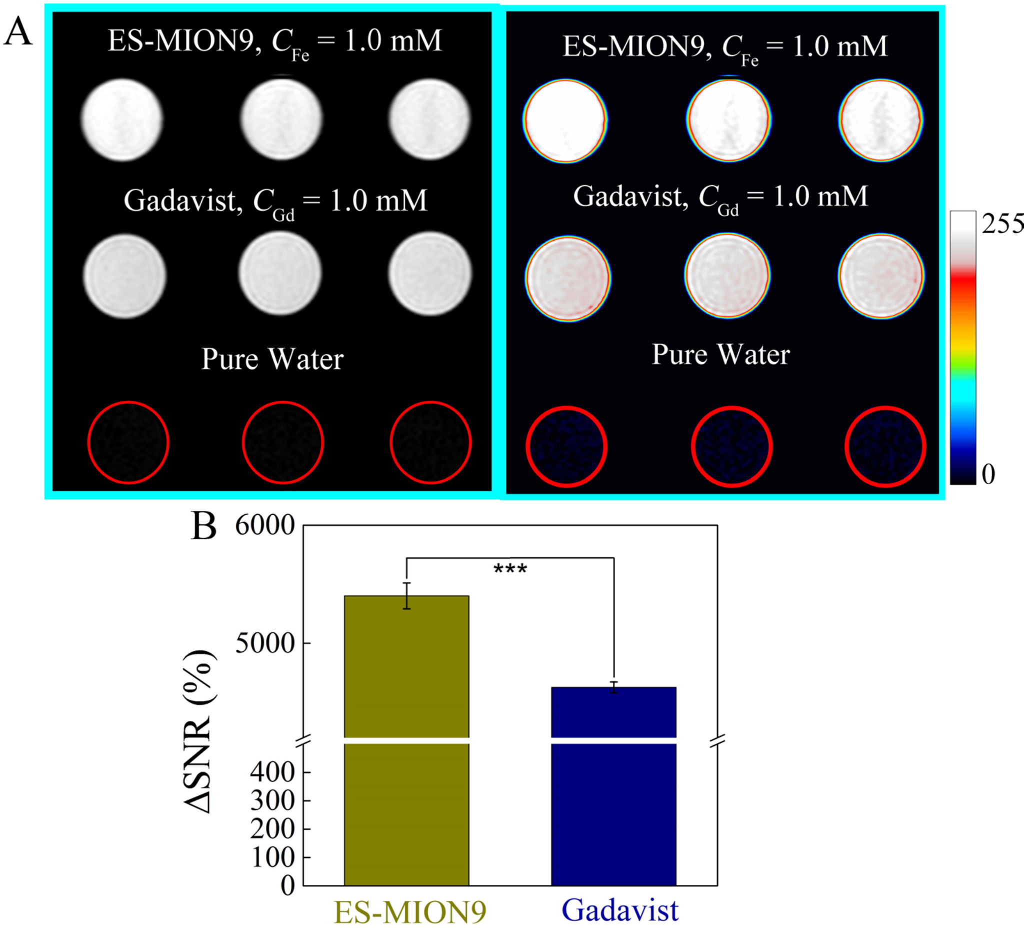

Fig. 3 **A** T_1-weighted MR images of ES-MION9 solutions ($C_{Fe} = 1.0$ mM) and commercial Gadavist solutions ($C_{Gd} = 1.0$ mM) compared with pure water (control). Magnetic field = 3.0 T. TE = 8.3 ms, TR = 200 ms. **B** ΔSNR of the MR images of ES-MION9 and Gadavist solutions, which is measured by the Image J. ***P < 0.001

[23]. Additional file 1: Fig. S8D shows the XRD of ES-MION9. Four characteristic peaks (2θ ≈ 30.0°, 35.2°, 42.8°, and 53.0°) match with the indices [(220), (311), (400), and (511)]. The crystal structure of ES-MION9 matches the pristine of Fe_3O_4, demonstrating the high crystalline purity of our ES-MION9. The field dependent magnetization curve (Additional file 1: Fig. S8E) indicates the ES-MION9 is superparamagnetic with 16.0 emu/g of saturation magnetization (M_s). All these results indicate that the ES-MION9 we synthesized is superparamagnetic Fe_3O_4 nanocrystals.

Because the M_s values of ES-MIONs increase with the increasing particle sizes [28], the small M_s value of ES-MION9 indicates its small particle size. In Eq. (4), the r is the magnetic core radius and M_s is the saturation magnetization. According to Eq. (4), both the extremely small particle size (3.7 nm) and small M_s (16.0 emu/g) lead to a very low r_2, which results in a very low r_2/r_1. Therefore, our exceedingly small ES-MION9 can be used as T_1 CA.

$$\frac{1}{T_2} = \frac{(256\pi^2\gamma^2/405)V^*M_S^2r^2}{D(1 + L/r)} \tag{4}$$

The high r_1 value of ES-MION9 is mainly due to the following two reasons: (1) ES-MION9 has a small particle size (3.7 nm), which gives ES-MION9 a larger specific surface area. In accordance with the mechanism of inner-sphere, larger specific surface area means there are more naked iron on ES-MION9 surfaces, which can fully interacts with hydrogen protons in H_2O molecules, resulting in a high r_1 value. (2) There are excessive carboxyl groups on ES-MION9 surfaces, and these carboxyl groups are derived from PASP, which greatly improves the water dispersion of ES-MION9. This leads to more H_2O in the inner sphere that can interact with the naked iron on the ES-MION9 surface, which causes a large number of bound H_2O (q) and mole fraction of H_2O coordinated to Fe (P_m) in Eq. (5) [16]. The large q and P_m result in a large r_1 value for ES-MION9.

$$\frac{1}{T_1} = \frac{q\,P_m}{T_{1m} + \tau_M} \tag{5}$$

The T_1/T_2 relaxation rate ($1/T_1$ or $1/T_2$) is plotted versus concentration for contrast agents, and the r_1 and r_2 values are calculated from the slopes of the corresponding fitting lines. T_1 CAs increase signal intensity of T_1 images by shortening the longitudinal relaxation time (T_1) of protons, which leads to high r_1 values. The Fe_3O_4 nanoparticles with size below 5.0 nm have low M_s values causing low r_2 values according to Eq. (4). Both high r_1 and low r_2 result in low r_2/r_1. Therefore, the 3.7 nm of ES-MION9 (< 5.0 nm) could be utilized for T_1 MRI [35, 36].

The hydrodynamic size (d_h) of ES-MION9 is 13.7 nm (Additional file 1: Fig. S9A), which is larger than renal filtration threshold (~ 8 nm). The slightly larger hydrodynamic diameter prolongs blood circulation time overcoming the limited MRI time window problem of commercial Gd chelates. The zeta potential of ES-MION9 was measured to be − 55.0 mV (Additional file 1: Fig. S9B), which is due to the presence of excessive carboxyl groups on the surface. Charge plays a key role in the behavior of intravenously injected nanoparticles and pharmacokinetics. For example, nanoparticles agglomerate under charge-mediated nonspecific binding to serum proteins. Sufficient negative charges can avoid the agglomeration of ES-MION9 while avoiding uptake of the nanoparticles by normal cells during blood circulation, resulting in more accumulated ES-MION9 in tumors. Additional file 1: Fig. S9C shows that the hydrodynamic diameter of ES-MION9 do not change significantly during storage in water, 10.0% FBS and 0.9% NaCl solution for 1 week, demonstrating the great stability of ES-MION9.

Additional file 1: Fig. S10 shows UV–vis absorption spectra for ES-MION1-11, which are similar with that of reported ES-MIONs stabilized with other polymers [23]. Additional file 1: Fig. S11 shows the FT-IR of PASP and ES-MIONN9. The stretching vibration peak of $-CH_2-$ at 1400.6 cm^{-1} can be seen from the FT-IR of PASP and ES-MION9, indicating the existence of PASP on the surface of ES-MION9 [37]. In addition, the stretching vibration peak of Fe–O at 604.5 cm^{-1} can be seen from the FT-IR of ES-MION9, but not in the FT-IR of PASP, indicating the existence of iron in ES-MION9. These results prove the successful synthesis of Fe_3O_4 [38]. Additional file 1: Fig. S12 presents the curves of thermogravimetric analysis (TGA) and differential thermogravimetry (DTG) for ES-MION9. As the temperature increases, the mass of ES-MION9 continues to decrease, and becomes stable at 37.8% of remaining mass. This is similar to 40.1% of Fe_3O_4 loading content for ES-MION9 measured by ICP. This result further demonstrates the existence of PASP on the ES-MION9 surface.

Cellular uptake, cytotoxicity assay and T_1-weighted imaging of cells

To evaluate the biosafety of ES-MION9, its cytotoxicity was examined by thiazolyl blue tetrazolium bromide (MTT) assay on MCF-7 cells (Human breast cancer cells) and 4T1 cells (Mouse breast cancer cells). Figure 4A, B shows that when the Fe concentration of ES-MION9 reaches 0.8 mM, the cell viability of MCF-7 cells and 4T1 cells was higher than 95.0%. This result indicates that ES-MION9 is almost not cytotoxic due to its biocompatible components (i.e., Fe_3O_4 and PASP). Although Gd^{3+} can cause nephrogenic systemic fibrosis and can be deposited in the human brain and body [39], Fig. 4A, B shows that the Gadavist is also non-toxic at the Gd concentration of 0.8 mM. That's because Gd^{3+} leads to long-term toxicity, which cannot be revealed in the short-term MTT assay.

To further demonstrate the non-cytotoxicity of ES-MION9, live/dead cytotoxicity analysis was used to evaluate the toxicity of ES-MION9 to 4T1 cells and MCF-7 cells (Additional file 1: Figs. S13, S14). The PBS treated cells were used as a control. Green dots represent live cells and red dots represent dead cells. Obviously, almost no dead cells are found for ES-MION9-treated 4T1 cells and MCF-7 cells, showing good biosafety of ES-MION9. That's because the main component aspartic acid (ASP) is one of the 20 essential amino acids and iron is one of the essential elements in the human body.

Figure 4C shows the LSCM images of 4T1 cells treated with ES-MION9@R6G. The red signal represents R6G@ES-MION9. After 2 h of co-incubation with 4T1 cells, lots of ES-MION9 nanoparticles were found inside the cells (Fig. 4C). The uptake of ES-MION9 by 4T1 cells was further investigated by flow cytometry. After 2 h of co-incubation with 4T1 cells, the fluorescence intensity (Additional file 1: Fig. S15A, B) of R6G-labeled ES-MION9 was almost two orders of magnitude higher than that of the control group with a statistical P value smaller than 0.001, indicating that ES-MION9 is easily taken up by 4T1 cells. The results of flow cytometry are consistent with the LSCM results. In addition, the T_1-weighted MR images (7.0 T) (Additional file 1: Fig. S16) show that ES-MION9-treated tumor cells have much stronger MRI signals compared to the control groups, and the MR signal also increases with the increase of incubation time from 1.0 to 2.0 h. These results demonstrate the excellent MR imaging capability of our ES-MION9 at the cellular level.

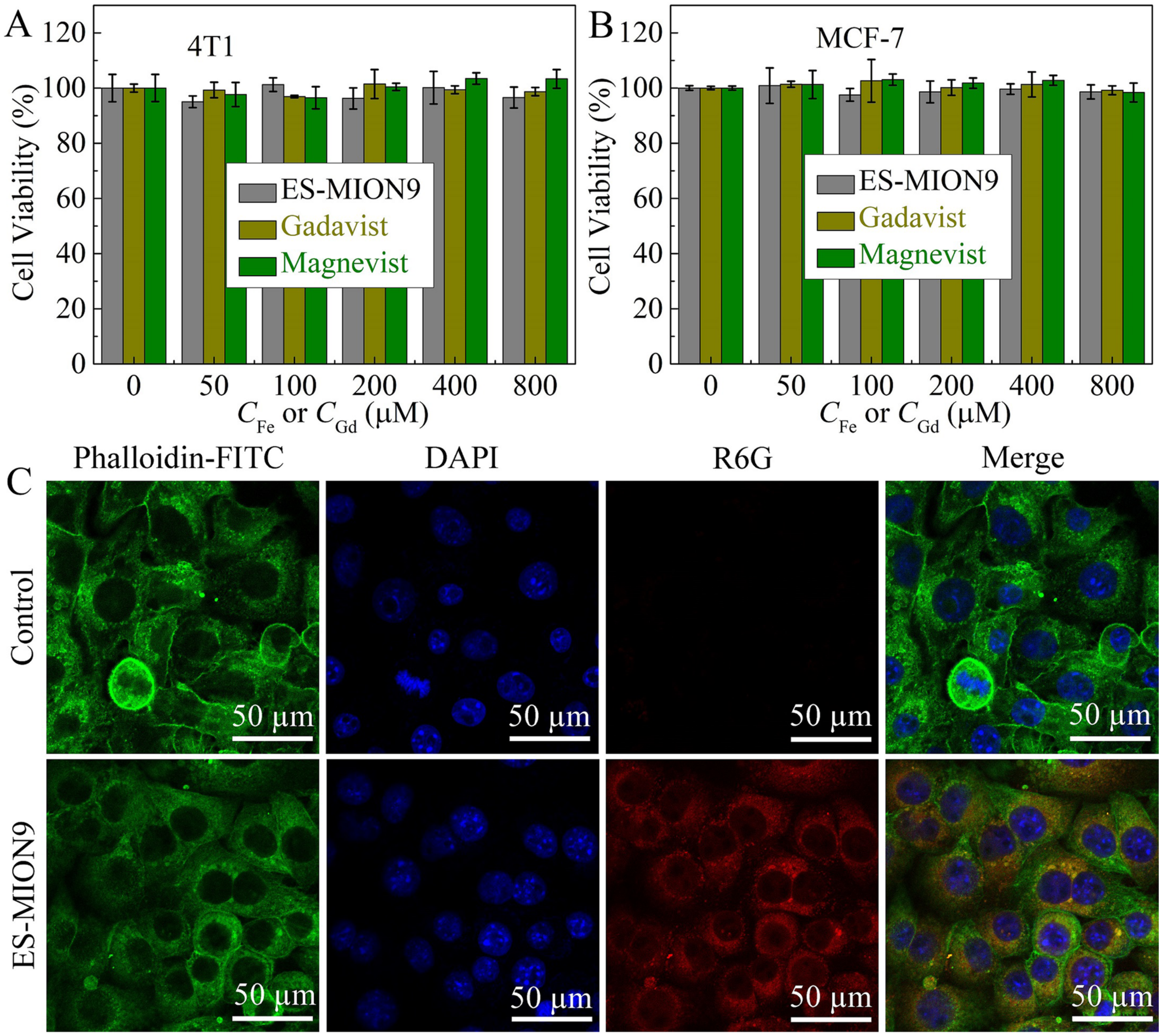

Fig. 4 **A**, **B** Cytotoxicity of ES-MION9, commercial Gadavist or Magnevist on 4T1 cells or MCF-7 cells. Mean ± SD, n = 4. **C** LSCM images of 4T1 cells treated with ES-MION9@R6G for 2.0 h. The cytoskeleton is green due to the phalloidin-FITC staining, and the nucleus is blue due to the DAPI staining

In vivo MR imaging

MRI can be used for soft tissue imaging, especially for tumor diagnosis. MR contrast agents can improve the signal-to-noise ratio and sensitivity of MRI. We tested the imaging ability of ES-MION9 in 4T1 tumor-bearing mice. 4T1 cells were seeded subcutaneously into BALB/c mice to build 4T1 tumor models. The commercial Gadavist and our ES-MION9 were i.v. injected into the 4T1 tumor-bearing mice for MR imaging (Fig. 5A, B). It can be seen from the MR images that after the administration of Gadavist or ES-MION9, the tumor becomes brighter than that of control (pre-injection), and reaches the brightest at 30 min or 3.0 h post-injection, respectively. MR images of different slices were obtained at each time point, and the brightest one of different slices at each time point was selected to characterize the MR imaging capabilities. Because the contrast difference between tumor and normal tissue is usually hard to be identified by the naked eyes, the signal changes in tumors at various time points after the administration of contrast agents are quantified using ΔSNR as shown in Fig. 5C, D, which is calculated according to the Eq. (6):

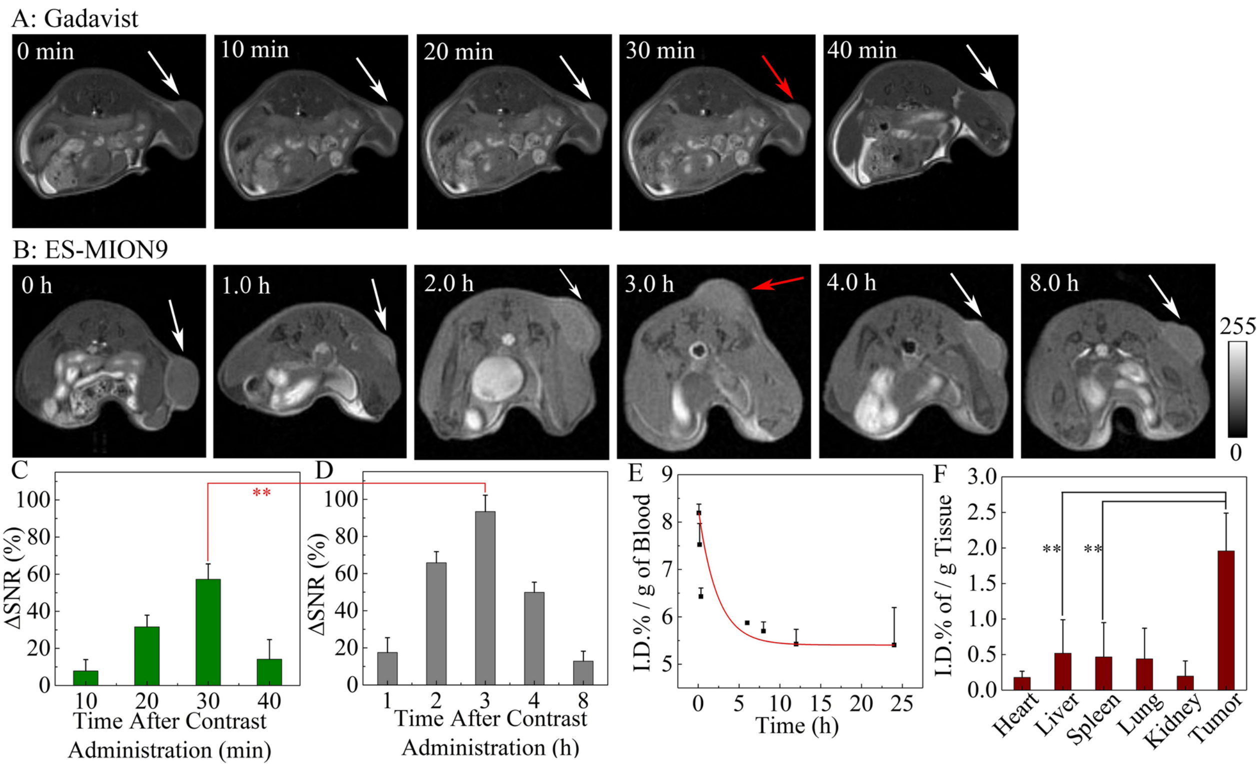

Fig. 5 **A**, **B**: T_1-weighted MR images of 4T1 tumor-bearing BALB/c mice with or without i.v. injection of Gadavist at 5.0 mg/kg of Gd dosage (**A**), or ES-MION9 at 5.0 mg/kg Fe dosage (**B**) under 7.0 T of magnetic field. **C**, **D** ΔSNR of the MR images for Gadavist (**C**), or ES-MION9 (**D**). **E**, **F** Blood clearance profile (**E**) and in vivo biodistribution of Fe level (**F**) in the 4T1 tumor-bearing BALB/c mice after i.v. injection of ES-MION9. Fe dosage is 5.0 mg/kg. $^{**}P < 0.01$

$$\Delta \mathrm{SNR} = \frac{(\mathrm{SNR}_{\mathrm{post}} - \mathrm{SNR}_{\mathrm{pre}})}{\mathrm{SNR}_{\mathrm{pre}}} \times 100\% \tag{6}$$

The ΔSNR value is up to 93.4% at 3.0 h after administration of ES-MION9 (Fig. 5D), which is significantly larger than that of the tumor at 30 min post-injection of Gadavist (57.2%, Fig. 5C). The above results demonstrate that our ES-MION9 can be utilized as a stronger MRI CAs compared with the clinically used Gd chelates.

Pharmacokinetics, biodistribution and biosafety evaluation in vivo

To verify that our ES-MION9 is more biocompatible and safer than Gadavist, the pharmacokinetics, biodistribution and biosafety were evaluated in vivo. Figure 5E shows that the blood half-life of ES-MION9 is about 2.3 h due to the small nanoparticle size (3.7 nm). The best time window for MRI in clinic is close to the half-life (10–15 min) of commercial Gd chelates, which is a little bit tight for MRI after administration of the Gd chelates [40]. The slightly longer half-life of our ES-MION9 overcomes the limited MRI time window problem of commercial Gd chelates.

To evaluate the biodistribution of ES-MION9 in vivo, the Fe contents in the heart, liver, spleen, lung, kidney and tumor of mice were measured at 0 h pre-injection and 12.0 h post-injection of ES-MION9, and the differences are shown in Fig. 5F. It is found the ES-MION9 accumulation inside tumors is very high compared with other normal tissues because of the enhanced permeability and retention (EPR) effect, which is the key reason for the highly enhanced MRI signal of tumors after ES-MION9 injection.

Additional file 1: Fig. S17 shows the representative optical microscopic pictures of the H&E-stained main organs from the normal mice without tumors (control), or that with i.v. injection of ES-MION9 ($C_{\mathrm{Fe}} = 5.0$ mg/kg). Compared with controls, ES-MION9-treated mice showed no obvious pathological abnormalities in major organs (heart, liver, spleen, lung, and kidney), indicating that our ES-MION9 does not lead to systemic toxicity.

Conclusions

In summary, in order to surmount the problems of commercial Gd chelates-based T_1 CAs, commercial MIONs-based T_2 CAs, and reported ES-MIONs-based T_1 CAs, a facile method based on co-precipitation was developed to synthesize biodegradable and biocompatible ES-MIONs with excellent water-dispersibility for T_1 MRI of tumors using PASP as the stabilizer. After optimization of the synthesis conditions, the final obtained ES-MION9 with a diameter of 3.7 nm has a high r_1 (7.0 ± 0.4 mM^{-1} s^{-1}) and a low r_2/r_1 (4.9 ± 0.6) at 3.0 T. The ES-MION9 has excellent water dispersibility due to the excessive carboxyl groups from PASP. The physical properties of ES-MION9 were further characterized by TEM, XRD, EDS, XPS, UV–vis, FT-IR, TGA, and magnetization curve. LSCM images and flow cytometry results prove the cellular uptake of ES-MION9 by endocytosis. The pharmacokinetics, and biodistribution of ES-MION9 in vivo demonstrate the better tumor targetability and MRI time window of ES-MION9 than commercial Gd chelates. T_1-weighted MR images of aqueous solutions, cells and tumor-bearing mice at 3.0 T or 7.0 T demonstrate that our ES-MION9 has a stronger MRI capability than the commercial Gd chelates. The MTT assay, live/dead staining of cells, and H&E-staining indicate the non-toxicity and biosafety of our ES-MION9. Consequently, the biodegradable and biocompatible ES-MION9 with excellent water-dispersibility is an ideal T_1-weighted CAs with promising translational possibility to compete with the commercial Gd chelates.

Materials and methods

Synthesis of ES-MIONs

In order to eliminate O_2, 20.0 mL and 0.5–4.0 mg mL^{-1} of PASP ($M_w = 7000$) solution was first bubbled using N_2 for 60 min. After that, the solution was heated to 100 °C under reflux. A Fe solution (0.4 mL, 125.0–500.0 mM $FeCl_3 + 62.5$–250.0 mM $FeSO_4$) was then rapidly charged to the above-mentioned PASP solution. Subsequently, $NH_3 \cdot H_2O$ (6.0 mL, 0.5–8.0%) was added under magnetic stirring. After 1.0 h, the reaction was stopped by cooling off. Finally, the synthesized ES-MIONs were purified via dialysis (Mw cut-off 8–14 kDa) in pure water for purification. An ICP-OES (iCAP PRO, Thermo Fisher Scientific, US) was used to determine the C_{Fe} of the ES-MIONs.

Synthesis of R6G@ES-MION9

At room temperature, 70.0 μL of Rhodamine 6G (100.0 μM) was added into 4.0 mL of ES-MION9 ($C_{Fe} = 2.8$ mM), and the mixture was magnetically stirred for 24.0 h. The prepared R6G@ES-MION9 solution was then centrifugally ultra-filtrated (Millipore, Mw cutoff 10 kDa) and washed utilizing ultrapure water for purification. Finally, the obtained R6G@ES-MION9 was resolved in ultrapure water (4.0 mL) and kept in 4.0 °C of refrigerator.

Supplementary Information

The online version contains supplementary material available at https://doi.org/10.1186/s12951-022-01562-y.

Additional file 1. The online version contains supplementary material available at https://jnanobiotechnology.biomedcentral.com.

Acknowledgements
Not applicable.

Author contributions
XQ, YX, and ZS conceptualized the study; XL, HZ, ZL, JF, YL, and LH carried out the experiments, and analyzed data; XL and HZ performed statistical analyses, prepared the figures, and wrote the manuscript draft. XQ, YX, and ZS participated in manuscript reviewing. ZS secured the funding. All authors read and approved the final manuscript.

Funding
This work was supported in part by the Guangzhou Key Research and Development Program of China (202103000094), Guangdong Provincial Natural Science Foundation of China (2021A1515010605), Zhejiang Provincial Natural Science Foundation of China (LR19E030001), and National Natural Science Foundation of China (51761145021).

Availability of data and materials
All data associated with this study are present in the paper and/or the additional file.

Declarations

Ethics approval and consent to participate
All animal procedures were performed in accordance with the Guidelines for Care and Use of Laboratory Animals of Southern Medical University and approved by the Animal Ethics Committee of Southern Medical University.

Consent for publication
All authors agree to publish this manuscript.

Competing interests
The authors declare no competing financial interest.

Received: 7 June 2022 Accepted: 15 July 2022
Published online: 30 July 2022

References

1. Poon C, Gallo J, Joo J, Chang T, Banobre-Lopez M, Chung EJ. Hybrid, metal oxide-peptide amphiphile micelles for molecular magnetic resonance imaging of atherosclerosis. J Nanobiotechnol. 2018;16:1–11.
2. Kawano T, Murata M, Kang JH, Piao JS, Narahara S, Hyodo F, Hamano N, Guo J, Oguri S, Ohuchida K. Ultrasensitive MRI detection of spontaneous pancreatic tumors with nanocage-based targeted contrast agent. Biomaterials. 2018;152:37–46.
3. Li X, Feng Q, Jiang X. Microfluidic synthesis of Gd-based nanoparticles for fast and ultralong MRI signals in the solid tumor. Adv Healthc Mater. 2019;8:1900672.
4. Zheng D, Yang K, Nie ZV. Engineering heterogeneity of precision nanoparticles for biomedical delivery and therapy. View. 2021;2:20200067.
5. Sitharaman B, Wilson LJ. Gadonanotubes as new high-performance MRI contrast agents. Int J Nanomed. 2006;1:291.

6. Wang Q, Liang Z, Li F, Lee J, Low LE, Ling D. Dynamically switchable magnetic resonance imaging contrast agents. Exploration. 2021;9:20210009.
7. Han Y, Zhou X, Qian Y, Hu H, Zhou Z, Liu X, Tang J, Shen Y. Hypoxia-targeting dendritic MRI contrast agent based on internally hydroxy dendrimer for tumor imaging. Biomaterials. 2019;213:119195.
8. Zhang M, Xing L, Ke H, He Y-J, Cui P-F, Zhu Y, Jiang G, Qiao J-B, Lu N, Chen H. MnO_2-based nanoplatform serves as drug vehicle and MRI contrast agent for cancer theranostics. ACS Appl Mater Interfaces. 2017;9:11337–44.
9. Wang F, Bae K, Huang Z, Xue J. Two-photon graphene quantum dot modified Gd_2O_3 nanocomposites as a dual-mode MRI contrast agent and cell labelling agent. Nanoscale Horiz. 2018;10:5642–9.
10. Haylor J, Dencausse A, Vickers M, Nutter F, Jestin G, Slater D, Idee JM, Morcos S. Nephrogenic gadolinium biodistribution and skin cellularity following a single injection of Omniscan in the rat. Invest Radiol. 2010;45:507–12.
11. Fidler J, Hough D. Hepatocyte-specific magnetic resonance Imaging contrast agents. Hepatology. 2011;53:678–82.
12. Ananta JS, Godin B, Sethi R, Moriggi L, Liu X, Serda RE, Krishnamurthy R, Muthupillai R, Bolskar RD, Helm L. Geometrical confinement of gadolinium-based contrast agents in nanoporous particles enhances T_1 contrast. Nat Nanotechnol. 2010;5:815–21.
13. Xue X, Bo R, Qu H, Jia B, Xiao W, Yuan Y, Vapniarsky N, Lindstrom A, Wu H, Zhang D. A nephrotoxicity-free, iron-based contrast agent for magnetic resonance imaging of tumors. Biomaterials. 2020;257:120234.
14. Mendichovszky IA, Marks SD, Simcock CM, Olsen OE. Gadolinium and nephrogenic systemic fibrosis: time to tighten practice. Pediatr Radiol. 2008;38:489–96.
15. Ledneva E, Karie S, Launay-Vacher V, Janus N, Deray G. Renal safety of gadolinium-based contrast media in patients with chronic renal insufficiency. Radiology. 2009;250:618.
16. Shen Z, Fan W, Yang Z, Liu Y, Bregadze VI, Mandal SK, Yung BC, Lin L, Liu T, Tang W. Exceedingly small gadolinium oxide nanoparticles with remarkable relaxivities for magnetic resonance imaging of tumors. Small. 2019;15:1903422.
17. Shu G, Chen M, Song J, Xu X, Lu C, Du Y, Xu M, Zhao Z, Zhu M, Fan K. Sialic acid-engineered mesoporous polydopamine nanoparticles loaded with SPIO and Fe^{3+} as a novel theranostic agent for T_1/T_2 dual-mode MRI-guided combined chemo-photothermal treatment of hepatic cancer. Bioact Mater. 2021;6:1423–35.
18. Zhao S, Yu X, Qian Y, Chen W, Shen J. Multifunctional magnetic iron oxide nanoparticles: an advanced platform for cancer theranostics. Theranostics. 2020;10:6278.
19. Na HB, Song IC, Hyeon T. Inorganic nanoparticles for MRI contrast agents. Adv Mater. 2009;21:2133–48.
20. Wang Z, Qiao R, Tang N, Lu Z, Wang H, Zhang Z, Xue X, Huang Z, Zhang S, Zhang G. Active targeting theranostic iron oxide nanoparticles for MRI and magnetic resonance-guided focused ultrasound ablation of lung cancer. Biomaterials. 2017;127:25–35.
21. Cai Z, Wu C, Yang L, Wang D, Ai H. Assembly-controlled magnetic nanoparticle clusters as MRI contrast agents. ACS Biomater Sci Eng. 2020;6:2533–42.
22. Reimer P, Balzer T. Ferucarbotran (Resovist): a new clinically approved RES-specific contrast agent for contrast-enhanced MRI of the liver: properties, clinical development, and applications. Eur Radiol. 2003;13:1266–76.
23. Shen Z, Chen T, Ma X, Ren W, Zhou Z, Zhu G, Zhang A, Liu Y, Song J, Li Z. Multifunctional theranostic nanoparticles based on exceedingly small magnetic iron oxide nanoparticles for T_1-weighted magnetic resonance imaging and chemotherapy. ACS Nano. 2017;11:10992–1004.
24. Shen Z, Wu A, Chen X. Iron oxide nanoparticle based contrast agents for magnetic resonance imaging. Mol Pharm. 2017;14:1352–64.
25. Xiang C, Zhong X, Yang W, Majeed MI, Wang J, Yu J, Hu J, Xu Z, Tan B, Zhang B, Yan W. Fe_3O_4 nanoparticles functionalized with polymer ligand for T_1-weighted MRI in vitro and in vivo. Polymers. 2019;11:882.
26. Liu Y, Yang Z, Huang X, Yu G, Wang S, Zhou Z, Shen Z, Fan W, Liu Y, Davisson M. Glutathione-responsive self-assembled magnetic gold nanowreath for enhanced tumor imaging and imaging-guided photothermal therapy. ACS Nano. 2018;12:8129–37.
27. Kim BH, Lee N, Kim H, An K, Park YI, Choi Y, Shin K, Lee Y, Kwon SG, Na HB. Large-scale synthesis of uniform and extremely small-sized iron oxide nanoparticles for high-resolution T_1 magnetic resonance imaging contrast agents. J Am Chem Soc. 2011;133:12624–31.
28. Shin TH, Kim PK, Kang S, Cheong J, Kim S, Lim Y, Shin W, Jung J-Y, Lah JD, Choi BW. High-resolution T_1 MRI via renally clearable dextran nanoparticles with an iron oxide shell. Nat Biomed Eng. 2021;5:252–63.
29. Wei Z, Jiang Z, Pan C, Xia J, Xu K, Xue T, Yuan B, Akakuru OU, Zhu C, Zhang G. Ten-gram-scale facile synthesis of organogadolinium complex nanoparticles for tumor diagnosis. Small. 2020;16:1906870.
30. Cai Y, Wang Y, Zhang T, Pan Y. Gadolinium-labeled ferritin nanoparticles as T_1 contrast agents for magnetic resonance imaging of tumors. ACS Appl Nano Mater. 2020;3:8771–83.
31. Liang H, Wu X, Zhao G, Feng K, Ni K, Sun X. Renal clearable ultrasmall single-crystal Fe nanoparticles for highly selective and effective ferroptosis therapy and immunotherapy. J Am Chem Soc. 2021;143:15812–23.
32. Shen Z, Song J, Zhou Z, Yung BC, Aronova MA, Li Y, Dai Y, Fan W, Liu Y, Li Z. Dotted core-shell nanoparticles for T_1-weighted MRI of tumors. Adv Mater. 2018;30:03163.
33. Chen Y, Song B, Tang X, Lu L, Xue J. Ultrasmall Fe_3O_4 nanoparticle/MoS_2 nanosheet composites with superior performances for lithium ion batteries. Small. 2014;10:1536–43.
34. Zhang J, Wang K, Xu Q, Zhou Y, Cheng F, Guo S. Beyond yolk-shell nanoparticles. Fe3O4@Fe3C core@shell nanoparticles as yolks and carbon nanospindles as shells for efficient lithium ion storage. ACS Nano. 2015;9:3369–76.
35. Lu Y, Xu YJ, Zhang GB, Ling D, Wang MQ, Zhou Y, Wu YD, Wu T, Hackett MJ, Hyo KB. Iron oxide nanoclusters for T_1 magnetic resonance imaging of non-human primates. Nat Biomed Eng. 2017;1:637–43.
36. Ling D, Park W, Park SJ, Lu Y, Kim KS, Hackett MJ, Kim BH, Yim H, Jeon YS, Na K. Multifunctional tumor pH-sensitive self-assembled nanoparticles for bimodal imaging and treatment of resistant heterogeneous tumors. J Am Chem Soc. 2014;136:5647–55.
37. Ahsan HM, Zhang X, Liu Y, Wang Y, Li Y, Li B, Wang J, Liu S. Stable cellular foams and oil powders derived from methylated microcrystalline cellulose stabilized pickering emulsions. Food Hydrocoll. 2020;104:105742.
38. Xu S, Wang J, Wei Y, Zhao H, Tao T, Wang H, Wang Z, Du J, Wang H, Qian J. Interfaces. In situ one-pot synthesis of Fe2O3@BSA core-shell nanoparticles as enhanced T1-weighted magnetic resonance imagine contrast agents. ACS Appl Mater Interfaces. 2020;12:56701–11.
39. Attari H, Cao Y, Elmholdt TR, Zhao Y, Prince MR. A systematic review of 639 patients with biopsy-confirmed nephrogenic systemic fibrosis. Radiology. 2019;292:376–86.
40. Huang CH, Nwe K, Al Zaki A, Brechbiel MW, Tsourkas A. Biodegradable polydisulfide dendrimer nanoclusters as MRI contrast agents. ACS Nano. 2012;6:9416–24.

Publisher's Note

Springer Nature remains neutral with regard to jurisdictional claims in published maps and institutional affiliations.

Ready to submit your research? Choose BMC and benefit from:

- fast, convenient online submission
- thorough peer review by experienced researchers in your field
- rapid publication on acceptance
- support for research data, including large and complex data types
- gold Open Access which fosters wider collaboration and increased citations
- maximum visibility for your research: over 100M website views per year

At BMC, research is always in progress.

Learn more biomedcentral.com/submissions

BMC